OAK RIDGE NATIONAL LABORATORY LIBRARIES

3 4456 0551614 4

ORNL/TM-6727

ornl

OAK
RIDGE
NATIONAL
LABORATORY

UNION
CARBIDE

# ORNL TNS Program: Evaluation of the Bundle Divertor

W. M. Wells

OAK RIDGE NATIONAL LABORATORY
CENTRAL RESEARCH LIBRARY
CIRCULATION SECTION
4500N ROOM 175
LIBRARY LOAN COPY
DO NOT TRANSFER TO ANOTHER PERSON
If you wish someone else to see this report, send in name with report and the library will arrange a loan.
UCN-7969 (3 9-77)

OPERATED BY
UNION CARBIDE CORPORATION
FOR THE UNITED STATES
DEPARTMENT OF ENERGY

Printed in the United States of America. Available from
National Technical Information Service
U.S. Department of Commerce
5285 Port Royal Road, Springfield, Virginia 22161
NTIS price codes—Printed Copy: A04; Microfiche A01

This report was prepared as an account of work sponsored by an agency of the United States Government. Neither the United States nor any agency thereof, nor any of their employees, makes any warranty, expressed or implied, or assumes any legal liability or responsibility for any third party's use or the results of such use of any information, apparatus, product or process disclosed in this report, or represents that its use by such third party would not infringe privately owned rights.

ORNL/TM-6727
Dist. Category UC-20 d

Contract No. W-7405-eng-26

FUSION ENERGY DIVISION

# ORNL TNS PROGRAM: EVALUATION OF THE BUNDLE DIVERTOR

W. M. Wells

Date Published - November 1979

Prepared by the
OAK RIDGE NATIONAL LABORATORY
Oak Ridge, Tennessee 37830
operated by
UNION CARBIDE CORPORATION
for the
DEPARTMENT OF ENERGY

OAK RIDGE NATIONAL LABORATORY LIBRARIES

3 4456 0551614 4

CONTENTS

LIST OF FIGURES ..... v
LIST OF TABLES ..... vii
LIST OF SYMBOLS ..... ix
ACKNOWLEDGMENTS ..... xi
ABSTRACT ..... xiii
INTRODUCTION ..... 1
1. PLASMA PHYSICS REQUIREMENTS ..... 3
2. BASIC MAGNETIC CONCEPTS ..... 7
2.1 MAGNETIC FIELD PERTURBATION ..... 7
2.2 APPROXIMATE METHOD FOR TREATING MAGNETIC FIELD PERTURBATION ..... 10
2.3 TREATING MAGNETIC FIELD PERTURBATION FOR TNS ..... 14
3. SCALING RELATIONS AND CONCLUSIONS FROM RESULTS OF OTHER STUDIES ..... 15
3.1 SCALING RELATIONS ..... 15
3.1.1 Current Scaling ..... 15
3.1.2 Resistance Scaling ..... 15
3.1.3 Power Scaling ..... 17
3.1.4 Current Density Scaling ..... 17
3.2 CONCLUSIONS FROM RESULTS OF OTHER STUDIES ..... 17
4. SHIELDING, CONDUCTOR, AND INSULATOR CONSIDERATIONS ..... 21
4.1 SHIELDING CALCULATIONS ..... 21
4.2 SHIELDING REQUIREMENTS ..... 21
4.2.1 Superconducting Coils ..... 21
4.2.2 Water-cooled Copper Coils ..... 22
4.2.3 Cryogenic Aluminum Coils ..... 22
4.3 INSULATION ..... 23
4.4 CONCLUSIONS ..... 24
5. ION AND ENERGY COLLECTION ..... 25
5.1 PREVIOUS CONCEPTS ..... 25
5.1.1 Solid Metals ..... 25
5.1.2 Liquid Lithium ..... 27
5.2 PROPOSED APPROACH ..... 30
5.2.1 The Droplet Cloud Concept ..... 30
5.2.2 Projected Performance ..... 30
5.2.3 Choice of Fluids ..... 32

6. CONCLUSIONS AND RECOMMENDATIONS ..... 33

REFERENCES ..... 35

APPENDIX 1: MINIMIZATION OF POWER CONSUMPTION IN HIGH PURITY REFRIGERATED ALUMINUM COILS ..... 37

REFERENCE ..... 39

APPENDIX 2: DETAILED PERFORMANCE ESTIMATES FOR DROPLET CLOUD CONCEPT ..... 43

1. METHOD OF ESTIMATING JET BREAKUP LENGTH ..... 43

2. METHOD OF ESTIMATING REQUIRED DENSITY AND SPACING OF DROPLETS ..... 44

3. METHOD OF ESTIMATING THE EFFECT OF LORENTZ FORCES ON THE DROPLETS ..... 44

4. METHODS OF ESTIMATING LIMITS ON DROPLET VELOCITY, TEMPERATURE, ION DOSE, AND HEAT FLUX ..... 47

REFERENCES ..... 51

FIGURES


1.1 Schematic of tokamak equipped with a bundle divertor ..... 4
2.1 Magnetic field lines diverted by a single vertical conductor ..... 8
2.2 Cross section showing effects of vertical conductor on field lines ..... 8
2.3 Adjacent dipole coils of opposite sense ..... 9
2.4 Comparison of large and small coils ..... 12
2.5 Curve defining the normalized toroidal field between null point and plasma centerline ..... 13
3.1 Current scaling relationship ..... 16
3.2 Bundle divertor configuration developed in Ref. 9 ..... 18
5.1 Hydrogen isotope ion collection data for various metals ..... 26
5.2 Gravity-driven flow ..... 28
5.3 Hartmann flow ..... 28
5.4 Droplet cloud concept, applied to TNS bundle divertor ..... 31
A1.1 Schematic representation of refrigeration cycle ..... 38
A1.2 General shape of resistivity ($1/\sigma$) vs temperature ($T_L$) curve at cryogenic temperatures ..... 40
A1.3 Resistivity of ultrapure aluminum at 4 T ..... 41
A2.1 Cross section of circular plasma opposite bundle divertor .... 45

TABLES

3.1 Parameters of Culham reactor (Ref. 9) and TNS-size power-producing reactor ..... 19
3.2 Parameters of TNS bundle divertor coils, scaled from Culham reactor coil parameters ..... 19
A1.1 Calculated values of Eq. (A1.3) for various temperatures ..... 42
A1.2 Energy consumption for different materials ..... 42
A2.1 Surface heat flux for two temperature limits ..... 50

## SYMBOLS

| | |
|---|---|
| $a$ | distance from null point to center of coil pair |
| $A$ | half the plate spacing for Hartmann flow |
| $B$ | magnetic field strength at the center of a circular filament coil |
| $B_{null}$ | magnetic field strength needed to create a null point at the desired location |
| $B_o$ | uniform magnetic field strength |
| $B_\perp$ | component of magnetic field perpendicular to flow plane |
| $B_T$ | toroidal magnetic field strength |
| $C$ | conductance ratio, $\sigma_w t_w/\sigma A$ |
| $d$ | jet diameter |
| $G$ | mass flux from surface |
| $I$ | coil current |
| $k$ | thermal conductivity |
| $K$ | constant |
| $L$ | linear dimension |
| $m$ | molecular weight |
| $M_\perp$ | Hartmann number, $B_\perp A \sqrt{\sigma/\eta}$ |
| $p$ | pressure |
| $p_\tau$ | pressure induced by surface tension |
| $\dot{q}''$ | surface heat flux |
| $Q$ | heat flow |
| $Q_L$ | low temperature component, ohmic heating contribution |
| $Q_H$ | high temperature component, total energy required |
| $r$ | coil radius |
| $r_d$ | droplet radius |
| $r_L$ | limiter radius |
| $R$ | resistance |
| $R_o$ | major radius of TNS (from pole of torus to plasma centerline) |
| $t$ | duration of heat flux |
| $t_c$ | thickness of droplet cloud |
| $t_w$ | thickness of wall |

| | |
|---|---|
| $T$ | absolute temperature |
| $T_H$ | high temperature |
| $T_L$ | low temperature |
| $v$ | velocity |
| $W$ | work |
| $We_j$ | Weber number for jet, $\rho_j(v^2d/\sigma)$ |
| $\alpha$ | half angle between divertor coils |
| $\beta$ | coefficient of performance |
| $\gamma$ | thermal diffusivity |
| $\Delta y$ | transverse displacement of a droplet |
| $\eta$ | viscosity |
| $\kappa$ | ratio of $\beta$ for real cycle and ideal cycle |
| $\lambda$ | dimensionless breakup length, $L/d$ |
| $\mu_o$ | magnetic permeability of vacuum |
| $\rho$ | density |
| $\rho_j$ | jet density |
| $\sigma$ | electrical conductivity |
| $\sigma_w$ | conductivity of wall |
| $\tau$ | surface tension |

ACKNOWLEDGMENTS

The author acknowledges major contributions by A. T. Mense to the section on plasma physics requirements and many helpful discussions with J. S. Watson on the droplet cloud concept and with M. A. Hoffman, of the University of California at Davis, on the jet breakup problem.

## ABSTRACT

This document provides an investigation of the feasibility of using a bundle divertor on the Reference Design for The Next Step (TNS) evolved at Oak Ridge National Laboratory (ORNL) during FY 1978. Additional information on the Reference Design and the FY 1978 Oak Ridge TNS activities can be found in the associated technical memoranda, ORNL/TM-6720–ORNL/TM-6726 and ORNL/TM-6728–ORNL/TM-6733.

# INTRODUCTION

The Next Step (TNS) represents that phase of fusion energy development in which the major emphasis would be directed toward engineering testing and demonstration. The objective of the TNS studies (initiated by the Department of Energy's Office of Fusion Energy) has been to define the characteristics and requirements of a facility dedicated to the engineering testing phase of fusion power development. For this reason, the TNS study results are providing a basis for defining an Engineering Test Facility (ETF). Because the scientific basis required for a TNS/ETF will first be available for the tokamak concept, the reactor core of the facility has been based on the tokamak concept. However, the commitment to an ETF with a reactor core based on the tokamak concept does not represent a commitment to tokamaks as the ultimate power reactor concept.

The TNS studies at Oak Ridge National Laboratory (ORNL) were initiated in FY 1977. During FY 1977 the Oak Ridge effort pursued scoping studies in three broad areas: plasma engineering, systems modeling, and program planning. Based upon the findings of the FY 1977 efforts, it was judged that continued activities in the Oak Ridge TNS program should be directed toward preconceptual design *with particular emphasis placed on engineering feasibility*. As a point of departure for the FY 1978 activities, a baseline design was selected, based on the systems modeling effort of FY 1977. The primary objective of our FY 1978 TNS effort has been to evolve the Baseline Design toward a preconceptual design. However, it is emphasized that the FY 1978 effort was not intended to lead to a completed preconceptual design. Therefore, the design resulting from this year's effort is referred to as a reference design, rather than as a preconceptual design.

Beyond these broad objectives, we quickly find ourselves addressing the question of whether a particular system should be included on TNS if it clearly does not meet the conditions of a commercial demonstration reactor (DEMO). The question should be answered on an individual basis for each system by evaluating the effect the system will have on the plasma behavior. The interaction of the plasma and a divertor (both in

general and for specific types of divertors) is poorly enough understood that this writer's view is: We must assume that there would be significant differences in the plasma behavior with and without a bundle divertor. Following this premise, we conclude that a bundle divertor should not be included on TNS if for some reason it is not feasible for DEMO. Thus, much of what follows addresses the question of technical feasibility for DEMO.

Structural considerations for the bundle divertor have not been dealt with for two reasons:

(1) Experience with the Divertor and Injection Tokamak Experiment (DITE) indicates no difficulty with structural feasibility.

(2) To deal conclusively with these considerations would require careful design, selection of the highest strength nonmagnetic materials, and detailed analysis of complex shapes. This level of treatment was deemed to be beyond the scope of this report.

# 1. PLASMA PHYSICS REQUIREMENTS

The successful production of power from fusion reactors depends on a number of factors.[1] One of the factors influencing the plasma performance is the concentration of $Z \neq 1$ impurities in the otherwise hydrogenic plasma. For the tokamak approach,[1] one possible technique for impurity control is the magnetic field divertor.[2] The experimental evidence from existing tokamak devices indicates that divertors do indeed prevent impurity buildup.[3,4] There may, however, be problems in extrapolating the presently implemented divertor designs to large-scale fusion reactors. The extrapolation of the divertor concept is the central theme of this paper.

Tokamak reactors as fusion power candidates have been discussed at length elsewhere;[1] only a brief description of the topology is warranted here. As shown in Fig. 1.1, the hot fusing plasma is contained in a central chamber by an appropriate magnetic field configuration. The magnetic field lines in this core region continually circle the machine and never wander far from a given constant pressure surface. To produce a divertor configuration, a coil pair is attached to the chamber (as shown in Fig. 1.1). These coils cause a "bundle" of magnetic field lines, or flux, to be pulled from the main confining zone and diverted into a remote collection chamber. The spatial boundary separating the main confining zone from the region where the magnetic field lines are diverted is called the separatrix surface. The hot plasma that diffuses from the core region across the separatrix and into the region of diverted field lines (sometimes called the scrape-off zone) follows these field lines into the remote collection chamber where particle collection and heat removal can be accomplished. It must be remembered that the success of the task requires that the collection process have a minimum impact on the purity of the main plasma core.

Recent studies undertaken at ORNL have addressed the problems involved in particle collection and power handling in this remote "burial chamber." Some of the initial findings from these studies are reported here.

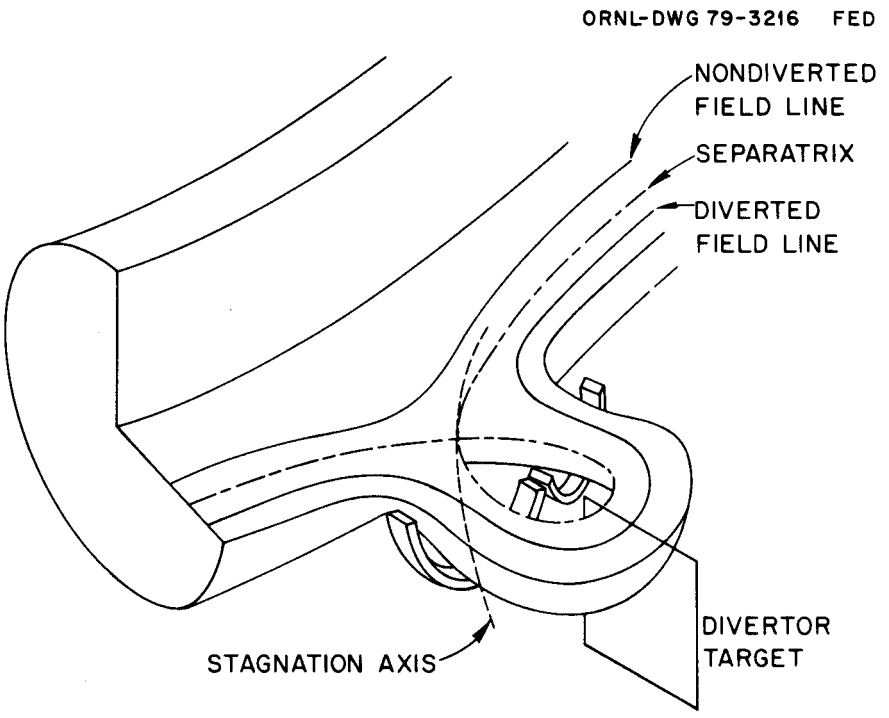


Fig. 1.1. Schematic of tokamak equipped with a bundle divertor. Principal features of the magnetic configuration are shown.

Before these problems can be addressed, the particle (electrons and ions) and energy flow rates to the burial chamber must be estimated. This task is within the domain of plasma physics, and a detailed description of how the numbers are computed is beyond the scope of this paper; for our purposes, it is sufficient to use a range of possible values. The ORNL TNS Reference Design is assumed to have a fusion power output of 1445 MW(th). Of this power, 226 MW shows up in the plasma and must be handled through heat transfer systems, either on the walls of the main confinement chamber or in the collection region of the burial chamber. As a conservative estimate, it is assumed that the entire 226 MW must be handled in the burial chamber. The particle flux to the burial chamber has been estimated, based on the experimental data on particle confinement times in the DIVA[4] and ALCATOR[5] tokamaks. The average particle fluxes leaving these devices are in the range of $10^{21}$-$10^{22}$ ions/$m^2$/sec. Multiplying these fluxes by the separatrix surface area of the ORNL TNS Reference Design, 314 $m^2$, gives particle flux rates in the range of $3 \times 10^{23}$-$3 \times 10^{24}$ particles/sec. The average energy of each particle that crosses the separatrix into the divertor scrape-off zone is in the range of 4.7 keV to 470 eV.

Two questions must be addressed:

(1) What is the ability of various materials to collect and retain the evident plasma ions (deuterium, tritium, and helium)?

(2) What is the maximum heat load the collector material is capable of tolerating?

In the study presented here, the collector material was chosen to be lithium. The extension to other materials is straightforward, provided the data are available.

# 2. BASIC MAGNETIC CONCEPTS

## 2.1 MAGNETIC FIELD PERTURBATION

A single vertical conductor placed near a toroidal magnetic field will divert a bundle of field lines, which then loop around the conductor as shown in Fig. 2.1. In order for this bundle to be diverted, the toroidal field must be reversed and there must be a null point at which the toroidal field is zero, as shown in Fig. 2.2. Figure 2.2 also shows the effect of the vertical conductor on the field lines. In zone 1, the field lines circle the conductor and do not travel around the torus (these are sometimes known as private lines). In zone 2, the field lines loop around the vertical conductor and travel around the torus. The outer boundary of zone 2 delineates the edge of the plasma as determined by a limiter. Clearly, zone 2 must avoid any structure; otherwise, that structure will assume the role of a limiter. In zone 3, the field lines do not loop around the conductor, but they deviate from the magnetic configuration without the vertical conductor. This deviation implies a perturbation in the toroidal magnetic field strength. The quantity most often used to express this perturbation is the toroidal magnetic field produced by the divertor at the plasma centerline, B, normalized to the basic toroidal magnetic field strength at that point, $B_T$. (This is discussed in detail in Sect. 2.2.)

These basic features apply in a general way for several different conductor configurations. Some of these configurations are examined in Ref. 6, which points out that the centerline perturbation caused by a single vertical conductor is excessive and can be lessened by the addition of more conductors, arranged to produce little or no effect on the field near the vertical conductor but to cancel the field farther from the vertical conductor. This type of behavior can also be obtained with a pair of adjacent dipole coils of opposite sense, as shown in Fig. 2.3. Near where the two coils touch, the field is determined almost entirely by the magnitude of the coil currents; farther from the coils, the field is small because the two dipoles are nearly of opposite sense. For a typical set of conditions,[6] the perturbation produced by a pair of circular coils is 1/33 of that produced by a vertical filament.

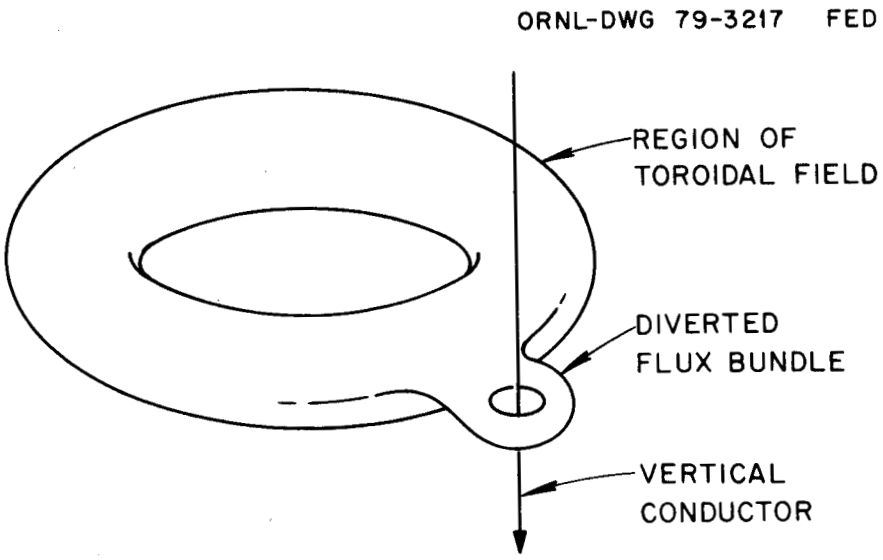


Fig. 2.1. Magnetic field lines diverted by a single vertical conductor.

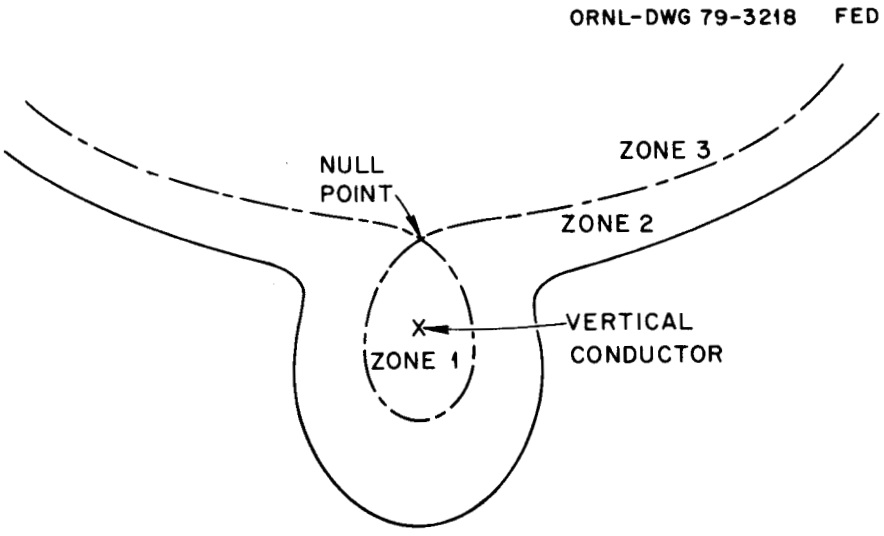


Fig. 2.2. Cross section showing effects of vertical conductor on field lines. At the null point, $B_T = 0$. Zone 1 contains "private" field lines; zone 2, the diverted field lines; and zone 3, field lines that deviate from the magnetic configuration without a divertor.

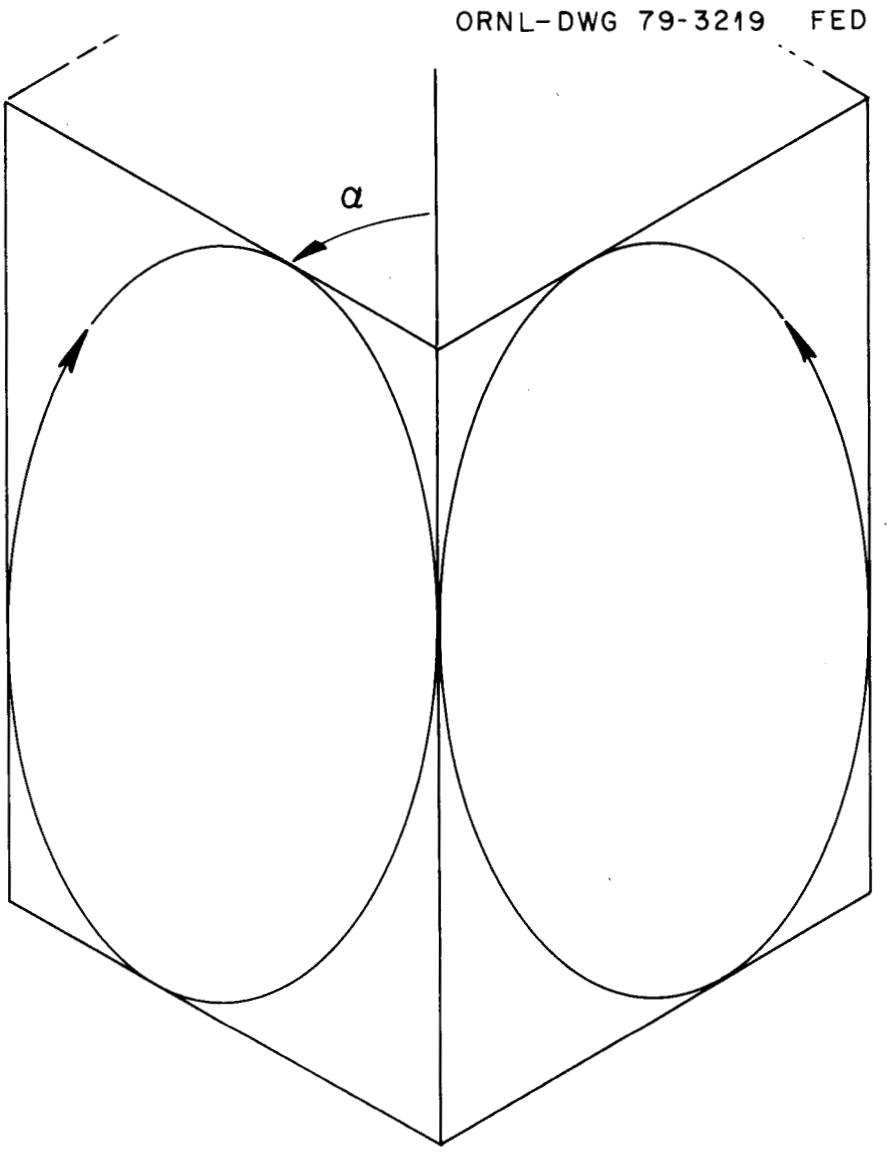


Fig. 2.3. Adjacent dipole coils of opposite sense.

## 2.2 APPROXIMATE METHOD FOR TREATING MAGNETIC FIELD PERTURBATION

The magnetic field strength produced at the center of a circular filament coil is

$$B = \frac{\mu_0 I}{2r} ,$$

where $\mu_0$ is the magnetic permeability of vacuum, I is the coil current, and r is the coil radius. If the size of the coil is increased (e.g., by increasing the radius, r), then the field strength at the center of the coil (the same scaled location) remains the same, provided the current is increased by the same factor. More generally, the scaled geometry of field lines and the scaled distribution of magnetic field strength for a given distribution of current elements are unique as the linear dimension scale factor is changed. It follows that if the field strength is normalized to that at a particular point in the scaled geometry of current elements, the normalized field strength distribution is also unique as a function of scaled position. These basic facts simplify the analysis of the perturbation discussed in Sect. 2.1 for particular coil configurations.

We assume that the desired location of the null point is fixed with respect to the toroidal plasma axis and with respect to the conductor array (this point is dealt with later). Producing the null point at a particular scaled location with respect to the coils is similar to normalizing at that point. A moment's thought reveals that such normalization results in a fractional perturbation of the preexisting toroidal field, where the value used for normalizing is the necessary field strength for creating a null point at the desired location, $B_{null}$. An important quantity to the plasma physicist is the perturbation on the plasma axis *normalized to the preexisting field at that point.* This renormalization is easily taken care of by the 1/R scaling of the basic toroidal field, $B_T$. We now see qualitatively that as the size of the coil pair decreases, the perturbation will also decrease. This situation

is illustrated in Fig. 2.4. The distance between the null point and the plasma axis is fixed. Thus, the small coils are a greater scaled distance from the plasma axis than the large coils, which leads to a reduced perturbation with the small coils.

Reference 7 shows that as the mean radius of the coil changes, the power, $I^2R$, is minimized when the distance from the null point to the center of the coil pair, a, is about equal to the coil radius (i.e., the null point is at a fixed scaled location as coil size changes). This was found to be the case for values of $\alpha$, the half angle between the coils (Fig. 2.4), from 50° to 90°. The coil cross section was 0.3 x 0.6 m with a = 1 m. Another necessary ingredient for the immediate purpose is supplied by Ref. 8, in which it is shown that the curve defining the normalized toroidal field between the null point and the plasma centerline is almost completely independent of the angle $\alpha$ over the range of 50° to 90°. A curve defining this field perturbation for filament coils is shown in Fig. 2.5.

In summary, the factors for considering magnetic field perturbation in the plasma region are

(1) the uniqueness of scaled field lines and $|B|$ distribution for a given conductor configuration,
(2) the same uniqueness when the field strength is normalized to the basic toroidal field at the null point,
(3) the minimizing of $I^2R$ for $a/r \cong 1$,
(4) the approximate uniqueness of the normalized $|B|$ curve between the null point and the plasma centerline for any reasonable value of $\alpha$, and
(5) the use of the fact that $B_T$ = const/R.

For filament-like coil pairs that have the null point located at a = r, the location required to produce a perturbation of 1.5-2% is reasonably explicit and the distance from null point to plasma axis is about 2.5-3 times the distance from null point to coil center. Further inspection of Fig. 2.5 reveals that trying to reduce field perturbation by enlarging the coils and backing them away is counterproductive, because this reduces the ratio of these two distances and increases the field perturbation at the plasma axis.

ORNL-DWG 79-3220 FED

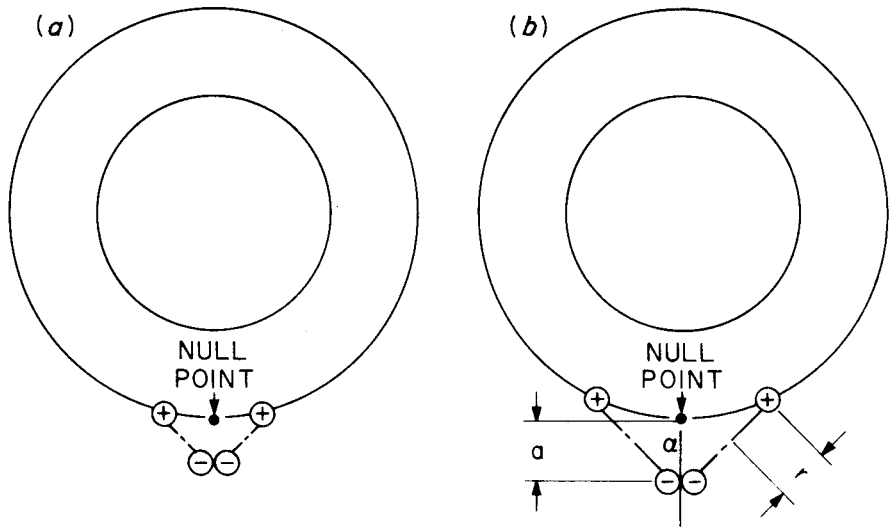


r IS COIL RADIUS

α IS HALF ANGLE BETWEEN COILS

a IS DISTANCE FROM NULL POINT TO CENTER OF COIL PAIR

Fig. 2.4. Comparison of large and small coils, where r is coil radius, α is half angle between coils, and a is distance from null point to center of coil pair.

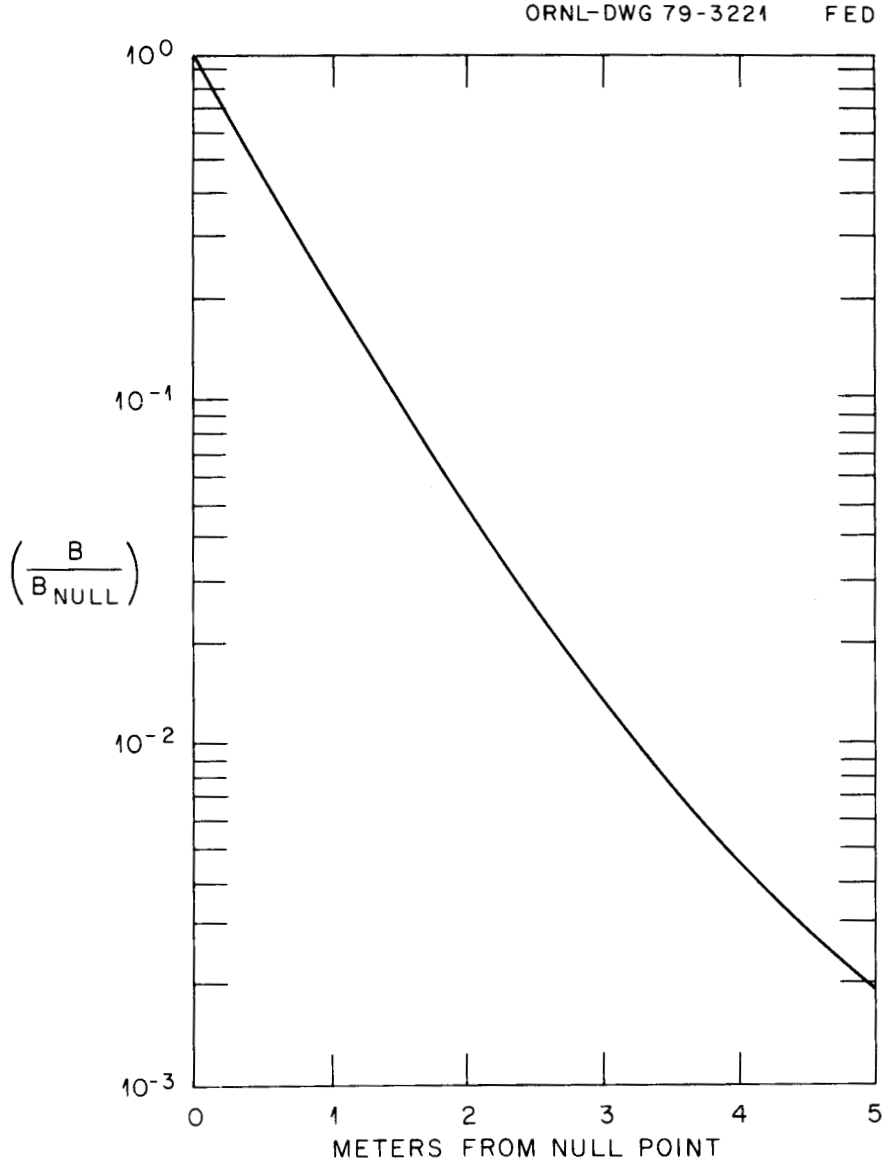


Fig. 2.5. Curve defining the normalized toroidal field between null point and plasma centerline, showing perturbation of toroidal field produced by bundle divertor coils with r = 1 m, $\alpha$ = 70°, and a = 1 m.

This discussion recognizes only the existence of the toroidal field. Reference 6 deals with a more realistic case that includes the magnetic field from the plasma current as well as vertical fields imposed to maintain plasma equilibrium. However, treatment of these nontoroidal fields is not necessary for preliminary purposes such as ours.

## 2.3 TREATING MAGNETIC FIELD PERTURBATION FOR TNS

For TNS, the device major radius, $R_0$, is 5.0 m, and the distance from the device center to the null point is 6.2 m. We assume that the centerline perturbation, defined as $|\Delta B|/[B_T(R_0)]$, is to be limited to 1.5% and use the scaling concepts defined in Sect. 2.2 to determine the size of the coil pair required. The perturbation limit relative to the preexisting field at the null point is

$$0.015 \times (6.2\ \text{m}/5\ \text{m}) = 0.0186\ .$$

Figure 2.5 indicates that this perturbation will occur 2.78 m from the null point. From the assumed dimensions, we know that the distance from the null point to the plasma axis is

$$a = 6.2\ \text{m} - 5\ \text{m} = 1.2\ \text{m}\ ,$$

so we may scale to obtain the actual coil radius,

$$r = (1.2\ \text{m}/2.78\ \text{m}) \times 1 = 0.43\ \text{m}\ .$$

This is a very small coil with inadequate room for shielding (as discussed in Sect. 4). However, increasing the coil size causes the centerline perturbation to increase rapidly. If, for this example, we increase the coil radius to r = 0.75 m and keep a = 1.2 m, we obtain a ratio of 1.6. The value of $B/B_{null}$ for this ratio is 7.5%, which implies a perturbation of

$$0.075 \times (5\ \text{m}/6.2\ \text{m}) = 0.060\ ,$$

or 6%, four times the initial limit of 1.5%.

# 3. SCALING RELATIONS AND CONCLUSIONS FROM RESULTS OF OTHER STUDIES

## 3.1 SCALING RELATIONS

Rigorous establishment of the scaling concepts presented below was considered to be beyond the scope of this report. Illustrative verification is used to convey the concepts.

### 3.1.1 Current Scaling

For a change in dimensional scale of the basic toroidal configuration, a change of the same scale in the divertor coils, and the same magnetic field strength, the bundle divertor current scales as the dimensional scale factor. The requirement is to produce a particular magnetic field at a fixed scale position, as illustrated in Fig. 3.1. The two cases shown represent bundle divertor coils with dimensional scales differing by a factor of 2, with the null point in the same scaled location. We postulate that the current requirement for case (b) is one-half that for case (a). For a simple case, we may verify this by taking the equation for the magnetic field, B, at the center of a circular filament coil,

$$B = \frac{\mu_0}{2} \frac{I}{r} .$$

Thus, if the scale factor increases by a factor of 2, then the coil current I must also increase by a factor of 2 to maintain the same field strength at the null point.

### 3.1.2 Resistance Scaling

Dimensionally, the electrical resistance can be described as

$$R = 1/\sigma L ,$$

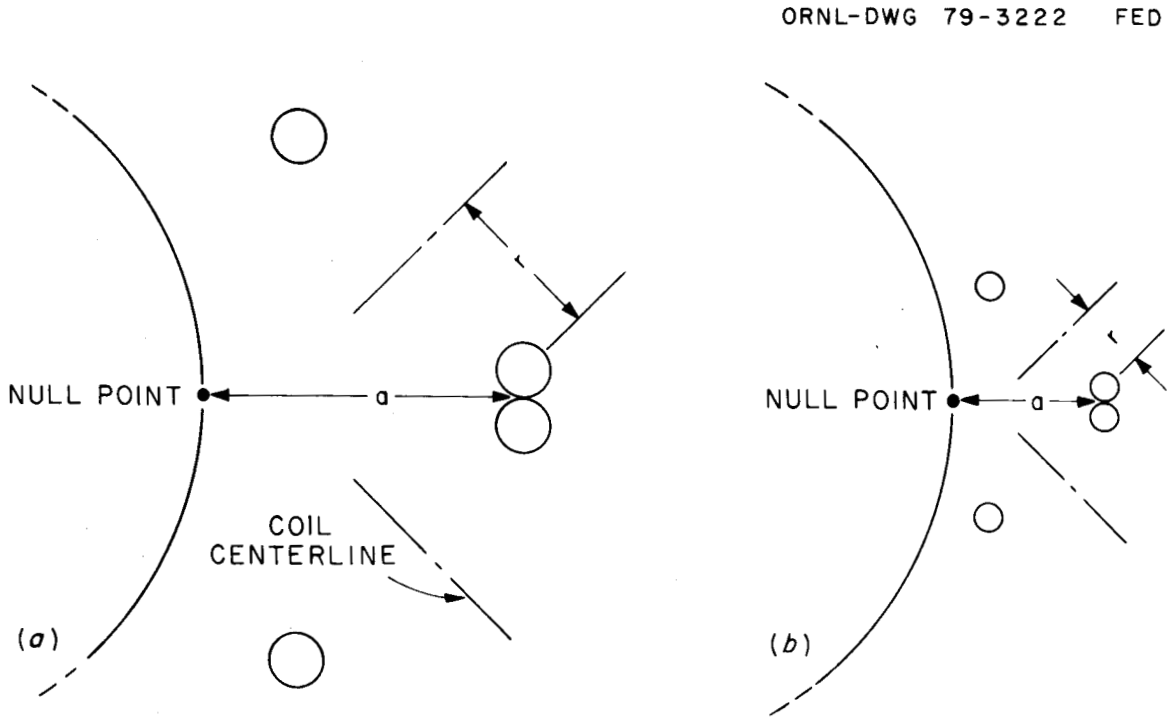


Fig. 3.1. Current scaling relationship. The coil radius of (a) is twice that of (b).

where L is the linear dimension and $\sigma$ is the electrical conductivity. From this, we may infer that the resistance of the bundle divertor coils varies inversely with the scale factor.

### 3.1.3 Power Scaling

We combine the current and resistance scaling relations to give a dimensional result of $I^2R$ and conclude that the power consumption of a coil set (within the context used here) varies directly with the scale factor.

### 3.1.4 Current Density Scaling

From the current scaling relation and area considerations, we conclude that the current density varies inversely with the scale factor.

## 3.2 CONCLUSIONS FROM RESULTS OF OTHER STUDIES

The most recent magnetic treatment of bundle divertors[9] has generated a distributed coil configuration that permits significantly ($\sim$3 times) thicker shielding than earlier studies,[7] as well as a reduction of the current density in the conductor. The improvement arises mainly from the way in which the cross-sectional area of the divertor coils is distributed, which deviates more from circular filament coils than earlier studies. The bundle divertor configuration developed in the study is shown in Fig. 3.2.

We have used the methods of Ref. 9 and the scaling relations of Sect. 3.1 to arrive at our conclusions about the bundle divertor coils for TNS. Table 3.1 lists pertinent parameters for the reference reactor of Ref. 9 and for a TNS-size power-producing reactor. As indicated by the table, the plasma regions of the two reactors are not quite geometrically similar, but they are similar enough that we treat them as though they were and scale on the values for horizontal semiaxis and toroidal field requirements. The scaled parameters for the TNS bundle divertor are compared with those of Ref. 9 in Table 3.2.

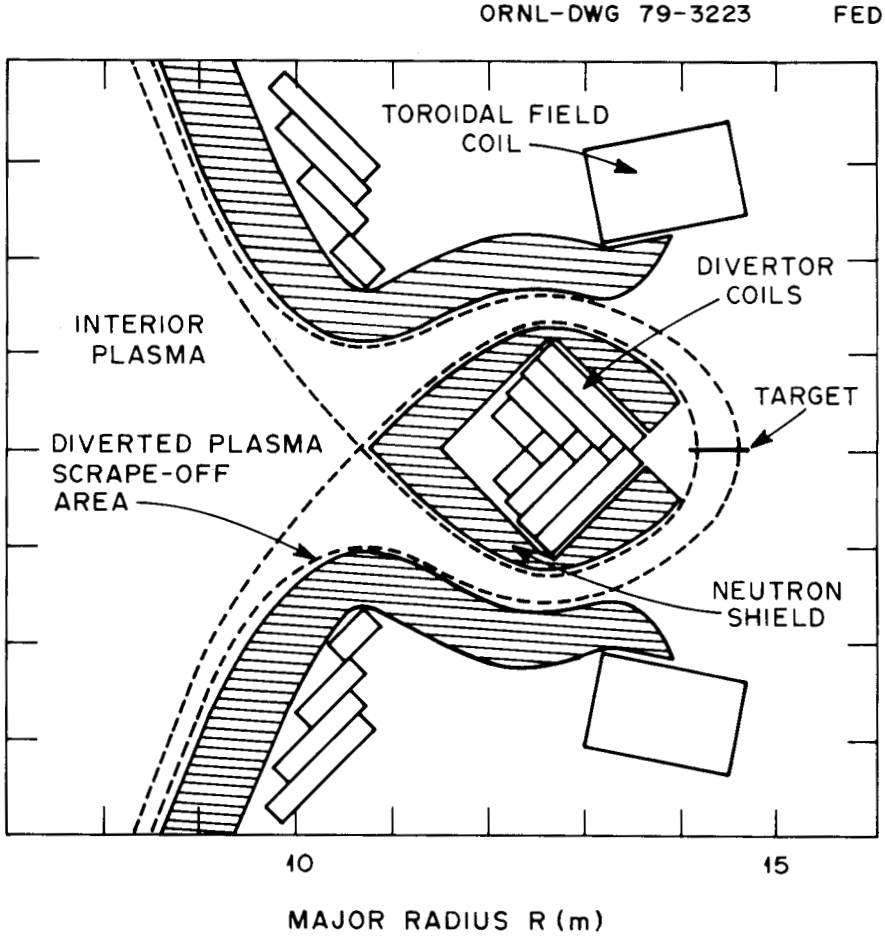


Fig. 3.2. Bundle divertor configuration developed in Ref. 9.

Table 3.1. Parameters of Culham reactor (Ref. 9) and TNS-size power-producing reactor

| | Culham reactor | TNS-size reactor |
|---|---|---|
| Electric power output | 2500 MW(e) | 500 MW(e) |
| Alpha particle power | 910 MW | 226 MW |
| Major radius | 7.4 m | 5 m |
| Plasma semiaxis (horizontal) | 2.1 m | 1.2 m |
| Plasma semiaxis (vertical) | 3.7 m | 1.92 m |
| Toroidal field at plasma centerline | 4.1 T | 5.28 T |

Table 3.2. Parameters of TNS bundle divertor coils, scaled from Culham reactor coil parameters

| | Culham reactor | TNS-size reactor |
|---|---|---|
| Mean coil radius, r | 1.8 m | 1.03 m[a] |
| Shield thickness | 0.75 m | 0.43 m[b] |
| Current density | 1.5 kA/cm$^2$ | 2.63 kA/cm$^2$ |
| Total power consumption for water-cooled copper coil (for a single bundle divertor) | 92 MW | 68 MW[c] |
| Percent of electrical output (for a single bundle divertor) | 3.7% | 14% |
| Maximum field in divertor coil | 7 T | 9 T[d] |

[a]Scaling calculation: 1.8 m x (1.2 m/2.1 m) = 1.03 m.

[b]Scaling calculation: 0.75 m x (1.2 m/2.1 m) = 0.43 m.

[c]Scaling calculation: 92 MW x (1.2 m/2.1 m) x (5.28 T/4.1 T) = 68 MW.

[d]Scaling calculation: 7 T x (5.28 T/4.1 T) = 9 T.

The most important conclusions from the scaling studies for the TNS-size reactor are

(1) the shield thickness does not permit the use of superconducting or cryogenic normal coils, and
(2) the power consumption of water-cooled copper coils is excessive.

The water-cooled copper divertor coils are reasonable for the large Culham reactor but unreasonable for the TNS-size reactor because the power production (for fixed power density) varies as the cube of the scale factor, while divertor power consumption varies linearly with the scale factor. This scaling strongly favors large reactors. However, it is important to realize that optimization of magnetic configurations — an area in which efforts to date have been far from exhaustive — may have a significant effect, and the negative conclusions reached above should be viewed with this in mind.

# 4. SHIELDING, CONDUCTOR, AND INSULATOR CONSIDERATIONS

## 4.1 SHIELDING CALCULATIONS

One of the more difficult constraints on the use of bundle divertor coils in power-producing reactors is the requirement of shielding the coils from neutron and other irradiation, which is in direct conflict with the need to have the coils close to the plasma (discussed in Sect. 2).

Several aspects of shielding in tokamak reactors are discussed in Ref. 10, including shielding for toroidal field (TF) coils. Although the geometry of the bundle divertor coils is somewhat more complex than that of TF coils (suggesting that for precise treatment three-dimensional calculations would be needed), for our purposes the one-dimensional treatment of Ref. 10 should be adequate.

The shield composition used in Ref. 10 consists of 30 cm of stainless steel nearest the plasma, followed by a layer of 50% stainless steel and 50% $B_4C$. To account for cooling, 10% of the volume is void. The results can be applied to specific cases with varying parameters (e.g., shield thickness).

The use of tungsten rather than stainless steel as the primary shielding material is evaluated in Ref. 11, which indicates that the same shielding can be achieved with 15% less thickness. The results below are obtained using the methods of Ref. 10. It is expected that substituting tungsten for stainless steel would improve the results by the order achieved in Ref. 11.

## 4.2 SHIELDING REQUIREMENTS

### 4.2.1 Superconducting Coils

The neutron wall loading for TNS is estimated at 2.4 $MW/m^2$. In order to restrict the reduction in critical current density of the superconductor to 10% over a 2-yr period, the shield thickness must be at least 0.85 m, and in order to restrict the resistivity of the copper

stabilizer in a superconducting coil to $3 \times 10^{-8}$ Ω cm, the shield thickness must be at least 0.95 m. Since even the lower requirement is almost twice the shield thickness of 0.43 m suggested by our scaling studies, we may effectively rule out superconducting coils.

### 4.2.2 Water-cooled Copper Coils

Given the TNS wall loading of 2.4 $MW/m^2$, we estimate that with a shielding thickness of 0.4 m, the neutron fluence in the insulator of a copper coil would reach $10^{21}$ $n/cm^2$ in 0.63 yr. While this is not acceptable for organic electrical insulation, it appears to be a reasonable limitation for ceramic insulator, as discussed in Sect. 4.3. Reference 12 indicates that the resistivity of water-cooled copper will increase by ∿10% at $10^{21}$ $n/cm^2$, also a reasonable limitation.

### 4.2.3 Cryogenic Aluminum Coils

Appendix 1 discusses the potential for reduction of power consumption through the use of very high purity aluminum in the 15K temperature range. At this temperature, with 99.999% pure aluminum in a magnetic field of ≤4 T, the power consumption (including refrigeration power) is about a factor of 9 lower than that for copper at room temperature. However, this conclusion does not take into account the effects of neutron irradiation,[13] and therein lies its fatal flaw.

The resistivity used to obtain optimum performance in Appendix 1 is $4.5 \times 10^{-9}$ Ω cm. If the resistivity were to increase to $22.5 \times 10^{-9}$ Ω cm, five times the optimum value, the power consumption advantage of operating at cryogenic temperatures would be substantially destroyed; the damage would have to be annealed by allowing the coil to warm to room temperature. According to Ref. 13, the neutron fluence required to produce this increase in the resistivity is $0.11 \times 10^{18}$ $n/cm^2$. As noted in Sect. 4.2.2, for a 0.4-m-thick shield the neutron fluence reaches $10^{21}$ $n/cm^2$ in 0.63 yr; linear interpolation is justified and leads to the conclusion that the coil must be annealed at room temperature every

36 minutes! While it is possible to imagine other technological problems associated with soft, high purity aluminum, the extreme sensitivity of the material to neutron irradiation and the absurd annealing requirement render such questions academic.

## 4.3 INSULATION

The maximum allowable radiation dose[10] for organic insulation (e.g., epoxy) with a lifetime of 12.5 yr is $\sim 4 \times 10^9$ rad. To prevent exceeding this dose in the 2.4-MW/m$^2$ wall loading of TNS, 1.0 m of shielding is required. For the 0.4-m-thick shield we propose, the radiation dose is $\sim 10^4$ times the maximum. Thus, we must consider inorganic insulation (e.g., ceramics).

Most of the data on neutron irradiation effects for ceramics are for temperatures well above those expected for insulators in water-cooled copper coils; however, based on these somewhat limited data and our present understanding of fundamentals, a neutron fluence of $10^{21}$ n/cm$^2$ should present no major problems for typical ceramics.[14] The requirements in terms of electrical and mechanical properties and swelling behavior are expected to be modest, which further supports our conclusion.

A technology base for the building of ceramic-insulated magnet coils is presently being established. A recent survey of the field[15] showed that beam-deflecting magnets using inorganic insulation have been built at all the accelerator laboratories, with the most common insulator being magnesium oxide.

The requirements for insulation in the bundle divertor coils are not especially stringent because:

(1) even if the insulator is poor by normal standards, copper is an extremely good conductor and current paths parallel to the basic one can be acceptable, and

(2) although ceramics are inherently brittle, it is conceptually possible to entrap the ceramic body so that cracking can be tolerated. The existing practice of using powdered ceramic is an extreme case that illustrates this point.

## 4.4 CONCLUSIONS

Given the 0.4-m-thick shielding proposed for the TNS bundle divertor coils, we conclude that neutron irradiation effects render both superconductors and cryogenic aluminum unacceptable and also prevent the use of organic insulation in water-cooled copper coils. Water-cooled copper coils with ceramic insulation can be used if they are replaced on an interval of $\sim$1 yr; in addition, advances in the technology of ceramic insulation are needed.

# 5. ION AND ENERGY COLLECTION

## 5.1 PREVIOUS CONCEPTS

### 5.1.1 Solid Metals

Data from experimental studies on the ability of various solid metals to collect and retain ions of hydrogen isotopes are presented in Ref. 16, which also contains original data of the same nature on liquid lithium. The data on solids were obtained by bombarding a target surface with ions ranging in energy from 3 to 30 keV, to a fluence of $2 \times 10^{19}$ ions/cm$^2$; the results are presented in Fig. 5.1. Additional data on titanium are presented in Ref. 17 for a single specimen cycled through the collection-thermal unloading cycle three times.

If we assume a power-on cycle of 20 min and size the target surface area to reach the saturation fluence of Ref. 16 in one cycle, we obtain a surface area of 300 m$^2$ and a heat load of 0.75 MW/m$^2$. The number of collection-thermal unloading cycles for TNS will be $\sim 10^5$. Obviously, active cooling methods having thermal and mechanical properties compatible with good structural materials will be required to perform this technologically formidable task.

Two approaches to the use of solid metals can be formulated. In the first, ion collection and material regeneration take place in a fixed location. This approach appears to be mechanically feasible. The second, however, involves moving belts or particle beds, and its feasibility is seriously questioned.

There are two other considerations that make the use of solid metals questionable. First, there is a substantial body of data (e.g., Ref. 18) dealing with the effects of hydrogen on the mechanical properties of metals (including two of the most likely candidates for this application, titanium and zirconium). In general, it has been shown that even a few atomic percent of hydrogen on a 1-cycle basis can cause degradation of mechanical properties; thus, it is unreasonable to expect that much higher concentrations of hydrogen for $10^5$ cycles will leave the construction material in an acceptable condition. Second, the

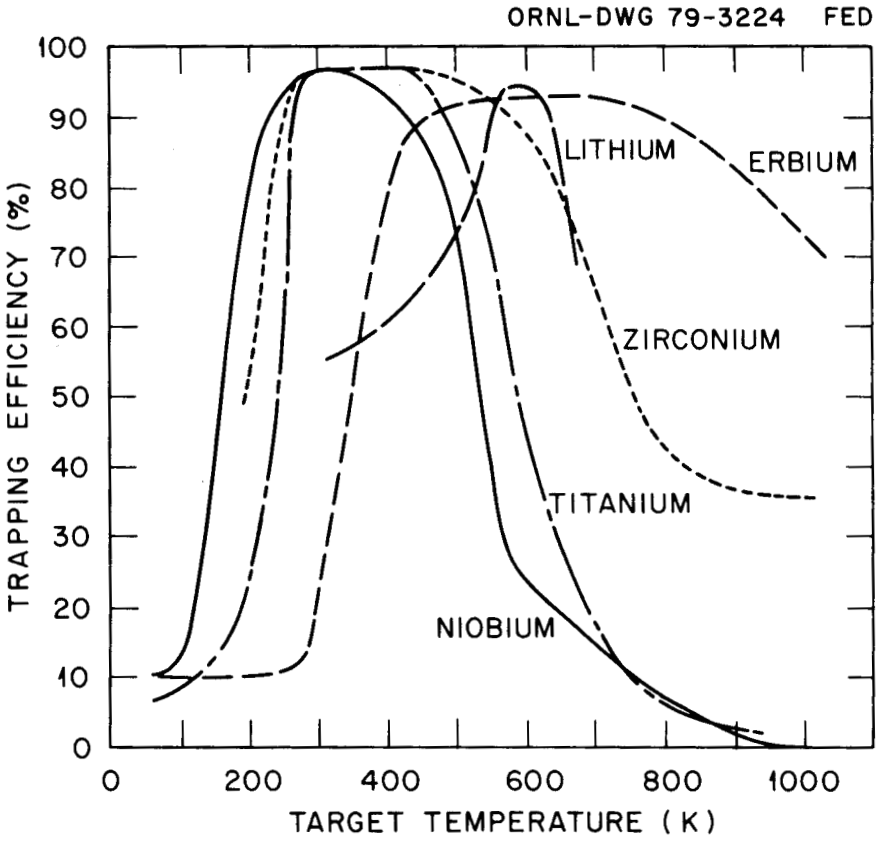


Fig. 5.1. Hydrogen isotope ion collection data for various metals.

removal of deuterium from samples subjected to ion implantation has been shown to require several hours at temperatures of 800-1000°C.[17] This appears to be far from acceptable for TNS.

### 5.1.2 Liquid Lithium

It is clear that the ability to pump the working medium as a fluid would have strong advantages in the areas of cooling the medium and removing the deuterium and tritium for recycling. The use of liquid lithium for this purpose has been suggested in three proposals,[19-21] all based on incorporation into the poloidal divertor concept.

The existing poloidal divertor concepts require that the collection take place in a strong toroidal magnetic field, and this is the case in Refs. 19-21. However, this field can cause serious problems in the collection and removal process.

In order for the lithium to carry out its ion target role, a free surface of the liquid must be available and the flow velocity must be sufficient to carry away heat and trapped ions. Reference 19 suggests that the lithium flow be a gravity-driven, free surface flow on a metal sheet; Refs. 20 and 21 also suggest gravity-driven flow but introduce constraint by capillary action via contact with a stainless steel screen. Figure 5.2 is a schematic illustration of gravity-driven free surface flow.

Liquid metal MHD studies began in the late 1930s, when Hartmann obtained an analytical solution for an incompressible conductive liquid flowing between flat plates with a magnetic field perpendicular to the flow, as shown in Fig. 5.3. Although Hartmann flow is generally presumed to be driven by pressure gradients, comparison of the boundary condition of gravity-driven free surface flow with that of Hartmann flow reveals enough similarity to permit an adequate approximation of the effects of the magnetic field on the gravity-driven flow.

The open channel flow of Fig. 5.2 can be seen to be the same as the flow occurring in half the channel width of Fig. 5.3. We approximate the stainless steel screen of Refs. 20 and 21 with a sheet having the

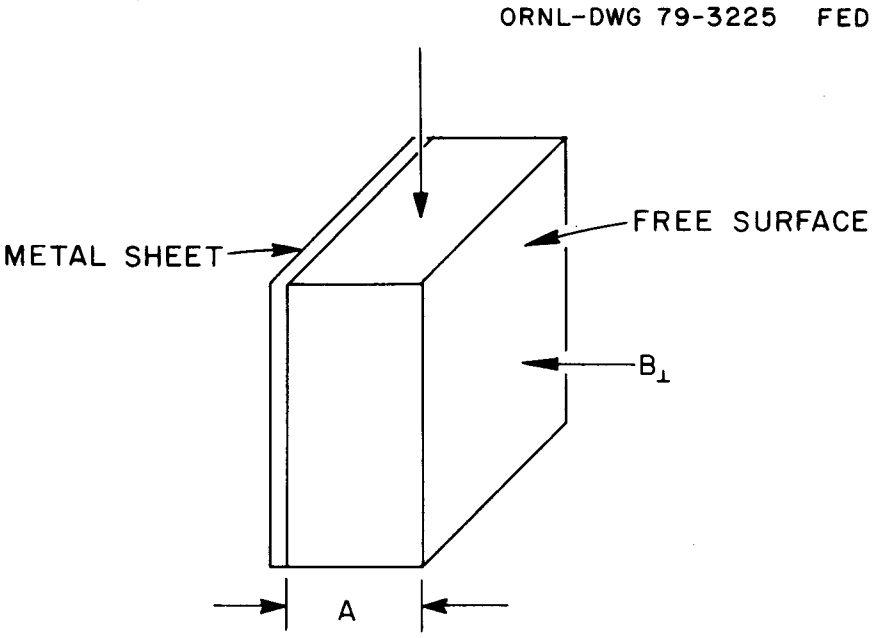


Fig. 5.2. Gravity-driven flow.

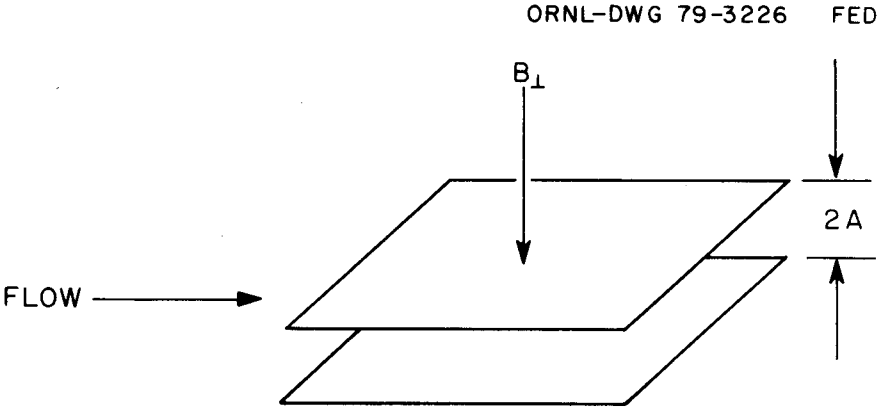


Fig. 5.3. Hartmann flow.

same cross-sectional area (to provide the same electrical resistance in order to determine the current flow). The pertinent equations for Hartmann flow are presented in Ref. 22 and may be written as

$$\frac{dp}{dx} = \frac{\eta v}{A^2}\left(\frac{M^2 \tanh M}{M - \tanh M} + \frac{M^2 C}{1 + C}\right) , \tag{1}$$

where p is the pressure, dp/dx is the pressure gradient in the direction of the flow, $\eta$ is the viscosity of the fluid, v is the velocity, A is half the plate spacing, $M_\perp$ is the Hartmann number,

$$M_\perp \equiv B_\perp A \sqrt{\sigma/\eta} ,$$

C is the conductance ratio,

$$C \equiv (\sigma_w t_w)/\sigma A ,$$

$B_\perp$ is the component of the magnetic field perpendicular to the flow plane, $\sigma$ is the electrical conductivity, $\sigma_w$ is the electrical conductivity of the wall (or plate), and $t_w$ is the wall thickness.

The value of A is taken as 1 mm, which is representative of the three proposals.[19-21] The pressure gradient, dp/dx, is taken to be the hydrostatic gradient, which is equal to the density by weight of lithium. Lithium properties are taken from Ref. 23 and stainless steel properties from Ref. 24.

Using this information and Eq. (1), we calculate the achieved flow velocity as 0.17 m/sec, a factor of 24 lower than the 4-m/sec velocity typical of Refs. 19-21. This calculation strongly suggests that the proposed approach of gravity-driven flow with constraint to a boundary wall (or screen) is not feasible. Additional questions about this approach include the stability of such a flow, the feasibility of collection of the flow in a strong magnetic field once it has traversed the intended gravity-driven region, and the problems of MHD flow in the necessary supply and return ducts.

## 5.2 PROPOSED APPROACH

### 5.2.1 The Droplet Cloud Concept

Our search for a means to avoid the severe difficulties with MHD flow discussed in Sect. 5.1 has resulted in a proposal to induce high velocity flow in a region nearly free of magnetic field, as illustrated in Fig. 5.4. The lithium flow leaves the nozzles as jets which are expected to break up into droplets (see Appendix 2) shortly after they leave the nozzles, forming a droplet cloud. As this cloud enters the high magnetic field region, the velocity of the droplets is uniform, there is no wall bounding the droplets, and the only Lorentz forces that arise are caused by nonuniformity of the magnetic field. In the high field region, ions impinge on the droplet cloud, are captured, and have their kinetic energy converted to heat. The droplets then leave the high field region and are collected; the resulting lithium stream is processed to remove heat and the collected hydrogen isotopes, which are returned to the plasma.

The success of this approach depends on having regions that are nearly free of magnetic field in which to form the jets and droplets and collect the lithium. The bundle divertor concept,[6,9] as illustrated in Fig. 5.4, clearly meets this requirement.

### 5.2.2 Projected Performance

It is assumed that the jets are formed outside the magnetic field at a pressure of 6.89 MPa (1000 psi). Under these conditions, and assuming a lossless conversion of pressure into kinetic energy, the jet will break up into 0.25-cm-diam droplets with a velocity of 166 m/sec slightly less than 1 m from the nozzle. If each droplet occupies 1% of the volume of a cube of space, the edge dimension of each cube will be 0.94 cm, and the droplet cloud must be 75 cm thick in order to intercept 99% of the collimated ions.

In passing through the target area, the droplet velocity will decrease by $1.2 \times 10^{-5}$ m/sec from the initial 166-m/sec velocity. The tendency toward disruption of the droplet is negligible compared to the

ORNL-DWG 79-3249 FED

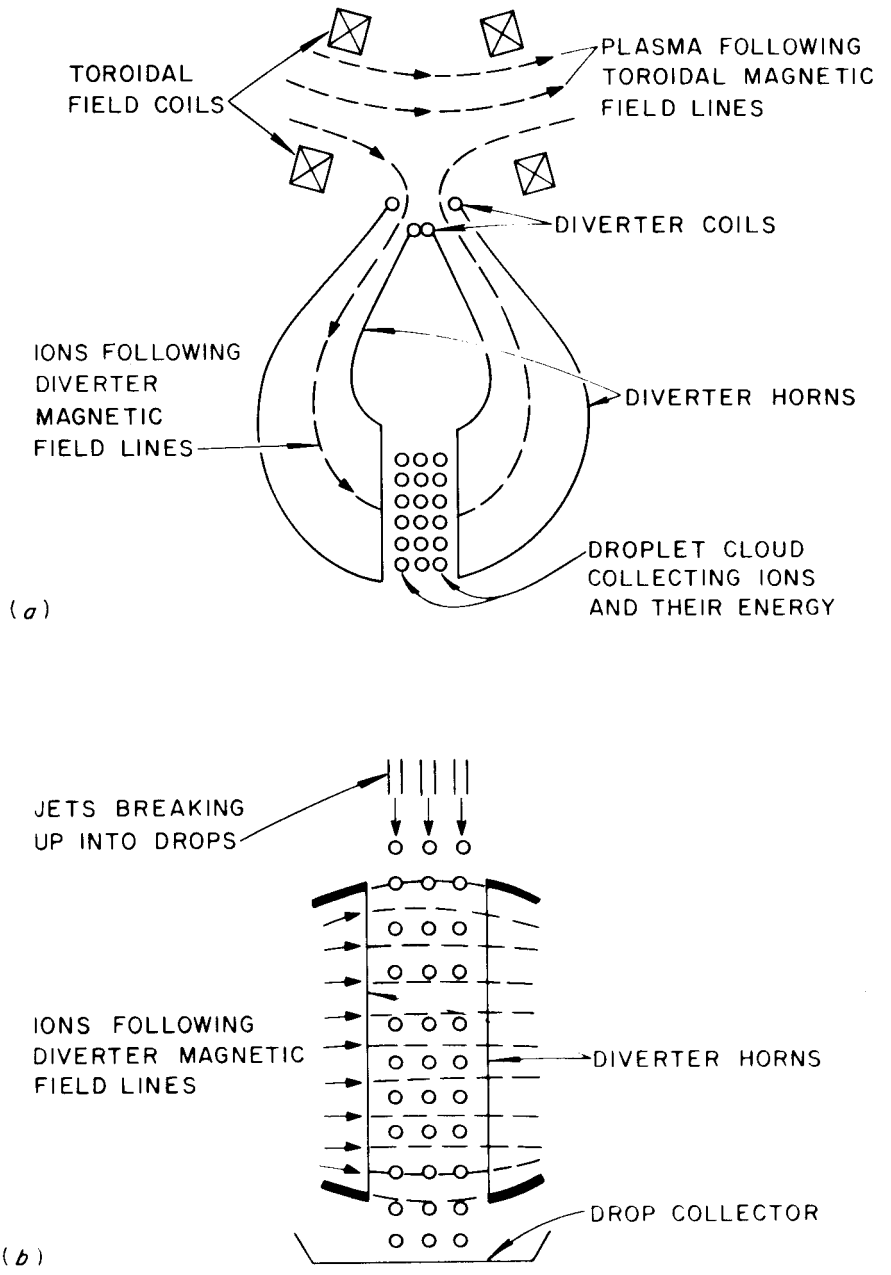


Fig. 5.4. Droplet cloud concept, applied to TNS bundle divertor. Regions of low magnetic field are available for jet formation and lithium collection. The size of the target area can be varied by using the expander coils.

surface tension force, and transverse deviation from a ballistic path is completely negligible. The peak temperature was taken to be 500°C, and the ion absorption dose is 1.1% of saturation for each pass of the droplets. Given these estimates (which are supported by analyses detailed in Appendix 2), a heat flux absorption capability of 1 $kW/cm^2$ appears easy to achieve and a value as high as 8 $kW/cm^2$ may be feasible.

### 5.2.3 Choice of Fluids

It has been strongly suggested that the fluid should be a hydride former, although consideration of ion trapping in some metallic solids that are not hydride formers indicates that this may not be necessary. As a case in point, the trapping of deuterium ions in stainless steel has been measured at $>10^{17}$ $ion/cm^2$ (Ref. 25). Presumably, this trapping occurs when energetic ions are embedded in the stainless steel. When fast moving liquid droplets impinge on the collection structure, the drops break up. This may tend to free hydrogen isotopes that are not chemically held and that would otherwise have to diffuse out.

Another factor in the choice of fluids is the liquid's vapor pressure. Tin, one of the liquid metals having a lower vapor pressure, does not have a stable hydride. Molten salts are largely unevaluated beyond recognition of the fact that ion bombardment will cause their chemical decomposition.

The mechanical trapping of embedded ions and the droplet breakup probably contribute in a major way to the question of whether the droplet cloud scheme can pump helium. Basic factors suggest that the scheme can probably pump neutral hydrogen isotopes. While the equilibrium pressure over the hydride is higher than desired, pressure in the range of Sievert's law constant should be useful. These points need to be specifically addressed.

## 6. CONCLUSIONS AND RECOMMENDATIONS

The droplet cloud concept may be the only feasible approach to handling the large heat and ion fluxes in a divertor. In addition, for a TNS-size power-producing reactor, the outlook for using a bundle divertor is questionable, because

(1) the available shield thickness (0.4 m) does not permit the use of superconducting coils, and

(2) while ceramic-insulated, water-cooled copper coils with a relatively short (∿1-yr) replacement cycle appear technically feasible, the power consumption for a single divertor is ∿14% of the reactor's total electrical output, which may be excessive.

Both of these problems are ameliorated in larger reactors.

In connection with establishing the technical feasibility of a divertor for TNS, two areas are most important:

(1) The configuration of the divertor current elements and the magnetic field should be optimized. (For example, all the toroidal field coils should be treated as variables in an evaluation of the magnetic field.) The basic requirement is to minimize the effects of field perturbation on the plasma while diverting an acceptable bundle of field lines.

(2) The ion pumping performance of the droplet cloud scheme should be assessed. Probably foremost is the question of whether the trapping of energetic ions without chemical binding (e.g., alpha particles and liquid droplets) is a viable pumping method.

In addition, the areas of droplet collection, the degree to which magnetic fields can and should be reduced in the droplet formation and collection regions, and the jet breakup should be addressed.

## REFERENCES


1. D. Steiner and J. F. Clarke, Science 199, 1395 (1978).
2. A. T. Mense, *A Poloidal Divertor Model for Tokamak Fusion Reactors*, UMFDM-219, University of Wisconsin, Madison, Wisconsin (1977).
3. S. J. Fielding et al., *Proc. 8th European Conf. on Controlled Fusion and Plasma Physics*, Vol. 1, p. 36 (1977).
4. Y. Shinomura and H. Maeda, J. Nucl. Mater. 76&77, 45 (1978).
5. E. S. Marmar, J. Nucl. Mater. 76&77, 59 (1978).
6. P. E. Stott, C. M. Wilson, and A. Gibson, Nucl. Fusion 17, 481 (1977).
7. H. J. Crawley, *Proc. 9th Symp. on Fusion Technology*, p. 381 (1976).
8. H. J. Crawley (Culham Laboratory, Abingdon, England), "The Practical Feasibility of a Bundle Divertor," 1975 (unpublished).
9. A. D. Sanderson and P. E. Stott, J. Nucl. Mater. 76&77, 530 (1978).
10. M. A. Abdou, *Important Aspects of Radiation Shielding for Fusion Reactor Tokamaks*, ANL/FPP/TM-81, Argonne National Laboratory, Argonne, Illinois (April 1977).
11. M. A. Abdou, Nucl. Technol. 29, 7 (1976).
12. R. R. Coltman, Jr. (Oak Ridge National Laboratory), private communication, August 1978.
13. M. Nakagawa, K. Boring, P. Rosner, and G. Vogl, Phys. Rev. B 16(12), 5285 (1977).
14. Frank W. Clinard, Jr. (Los Alamos Scientific Laboratory, Los Alamos, New Mexico), private communication, November 1978.
15. R. D. Hay and E. J. Rapperport, *A Review of Electrical Insulation in Superconducting Magnets for Fusion Reactors (Final Report)*, Magnetics Engineering Associates, Cambridge, Massachusetts (April 1976).
16. G. M. McCracken and S. K. Erents, *Nuclear Fusion Reactors (Proc. British Nuclear Energy Society Conf.)*, p. 353 (1970).
17. I. Sheft, A. H. Reis, D. M. Gruen, and S. W. Peterson, J. Nucl. Mater. 59, 1 (1976).

18. I. M. Bernstein and A. W. Thompson (eds.), *Hydrogen in Metals*, American Society for Metals, Metals Park, Ohio, 1974.

19. *UWMAK I: A Wisconsin Toroidal Fusion Reactor Design*, p. III-D-1, UWFDM-68 (revised ed.), University of Wisconsin, Madison, Wisconsin (1974).

20. T. F. Yang, A. Y. Lee, and G. W. Ruck, *Westinghouse Compact Poloidal Divertor Reference Design*, WFPS-TME-042, Westinghouse Fusion Power Systems Department, Pittsburgh, Pennsylvania (August 1977).

21. Westinghouse Fusion Power Systems Department, *Fusion Power Actinide Burner Design Study*, EPRI-ER-481, Electric Power Research Institute, Palo Alto, California (May 1976).

22. M. A. Hoffman and G. A. Carlson, *Calculation Techniques for Estimating the Pressure Losses for Conducting Fluid Flows in Magnetic Fields*, UCRL-51010, Lawrence Radiation Laboratory, Livermore, California (February 1971).

23. J. O. Cowles and A. D. Pasternak, *Lithium Properties Related to Use as a Nuclear Reactor Coolant*, UCRL-50647, Lawrence Radiation Laboratory, Livermore, California (April 1969).

24. *Metals Handbook*, p. 314, American Society for Metals, Metals Park, Ohio (1958).

25. N. J. Freeman, I. D. Latimer, and N. R. Daly, Nature (London) 212, 1346 (1966).

# APPENDIX 1

## MINIMIZATION OF POWER CONSUMPTION IN HIGH PURITY REFRIGERATED ALUMINUM COILS*

We consider a refrigeration cycle represented in Fig. A1.1, where $Q_L$ is the low temperature input to the cycle and for this case is the ohmic heating contribution, w is the work, and $Q_H$ is the high temperature heat flow from the cycle and is also the total energy required. The coefficient of performance, $\beta$, is assumed to be $\kappa$ times that of an ideal reversible cycle, where $\kappa$ is the ratio of $\beta$ for the real cycle and the ideal cycle $[T_L/(T_H - T_L)$, where T is absolute temperature], and may be written as

$$\beta = \frac{Q_L}{W} = \frac{Q_L}{Q_H - Q_L} = \kappa \frac{T_L}{T_H - T_L} . \tag{A1.1}$$

We define $Q_L$ as $K/\sigma(T_L)$, where K is a constant and $\sigma$ is the conductivity and a function of $T_L$. Using this definition, we may write $Q_H$, which is the quantity we wish to minimize, as

$$Q_H = \frac{K}{\sigma}\left[\frac{1}{\kappa}\left(\frac{T_H}{T_L} - 1\right) + 1\right] . \tag{A1.2}$$

If we differentiate $Q_H$ and set it equal to zero, we obtain

$$\frac{d(1/\sigma)}{dT_L} = \frac{1}{\sigma T_L}\left[\frac{T_H/T_L}{(T_H/T_L) - (1 - \kappa)}\right] . \tag{A1.3}$$

---

*This argument applies only in the absence of neutron irradiation effects. As discussed in Sect. 4.2.3 of this report, for the assumed 0.4-m shield thickness these effects destroy the power consumption advantages.

ORNL-DWG 79-3227 FED

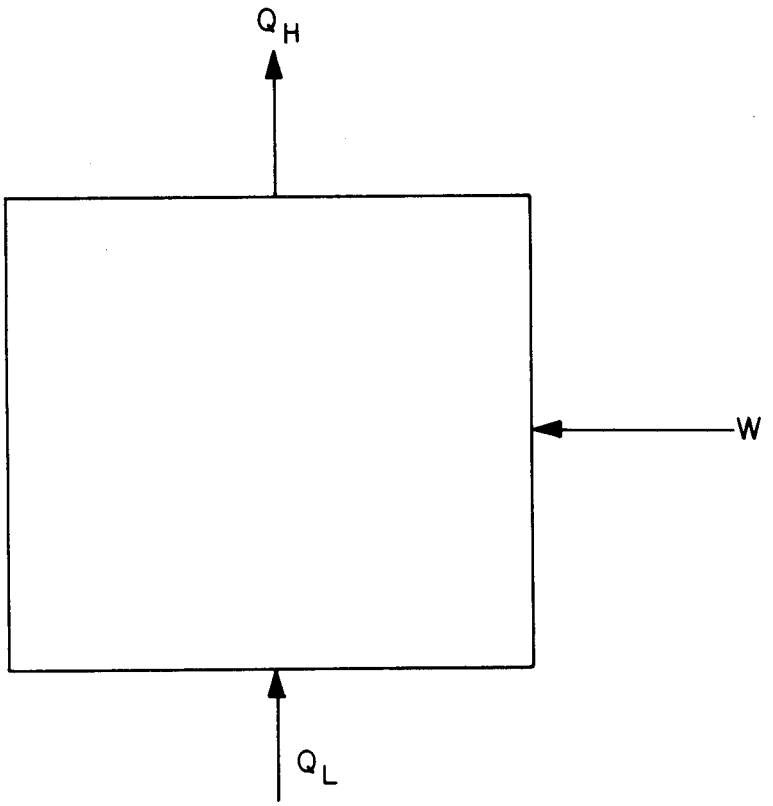


Fig. A1.1. Schematic representation of refrigeration cycle. $Q_H$ is the quantity to minimize.

For the reversible cycle ($\kappa = 1$),

$$\frac{d(1/\sigma)}{dT_L} = \frac{(1/\sigma)}{T_L} . \tag{A1.4}$$

Figure A1.2 shows the general shape of the $1/\sigma$ vs $T_L$ curve at cryogenic temperatures and indicates that Eq. (A1.4) is satisfied when the tangent to the curve passes through the origin. Data taken at 4 T are plotted in Fig. A1.3 (Ref. 1), and the tangent to the curve has been drawn and indicates an optimum temperature of $\sim$14.2K for a reversible cycle. This is very nearly the same as the operating temperature derived from Eq. (A1.3), as shown by the calculated values listed in Table A1.1. The values for $d(1/\sigma)/dT_L$ were obtained by measuring slopes. It is obvious that the optimum temperature for $\kappa = 0.3$ is only slightly greater than that for $\kappa = 1$ (the reversible case).

In Table A1.2, we compare the energy consumption of room temperature copper, room temperature aluminum, and cryogenic aluminum. We find that the energy consumption for cryogenic aluminum is 0.16 times that for room temperature copper and 0.11 times that for room temperature aluminum.

## REFERENCE

1. J. R. Purcell and R. B. Jacobs, Cryogenics 3, 109 (1963).

ORNL-DWG 79-3228 FED

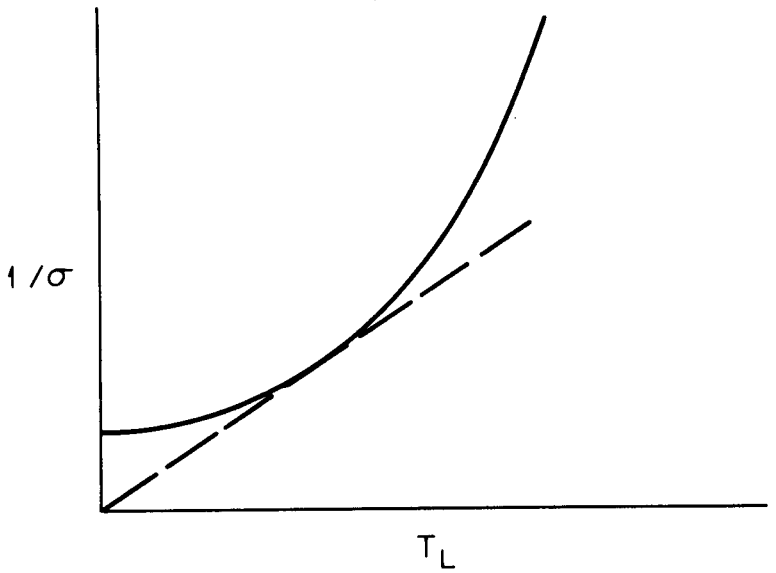


Fig. A1.2. General shape of resistivity ($1/\sigma$) vs temperature ($T_L$) curve at cryogenic temperatures. The dotted line indicates the tangent to the curve.

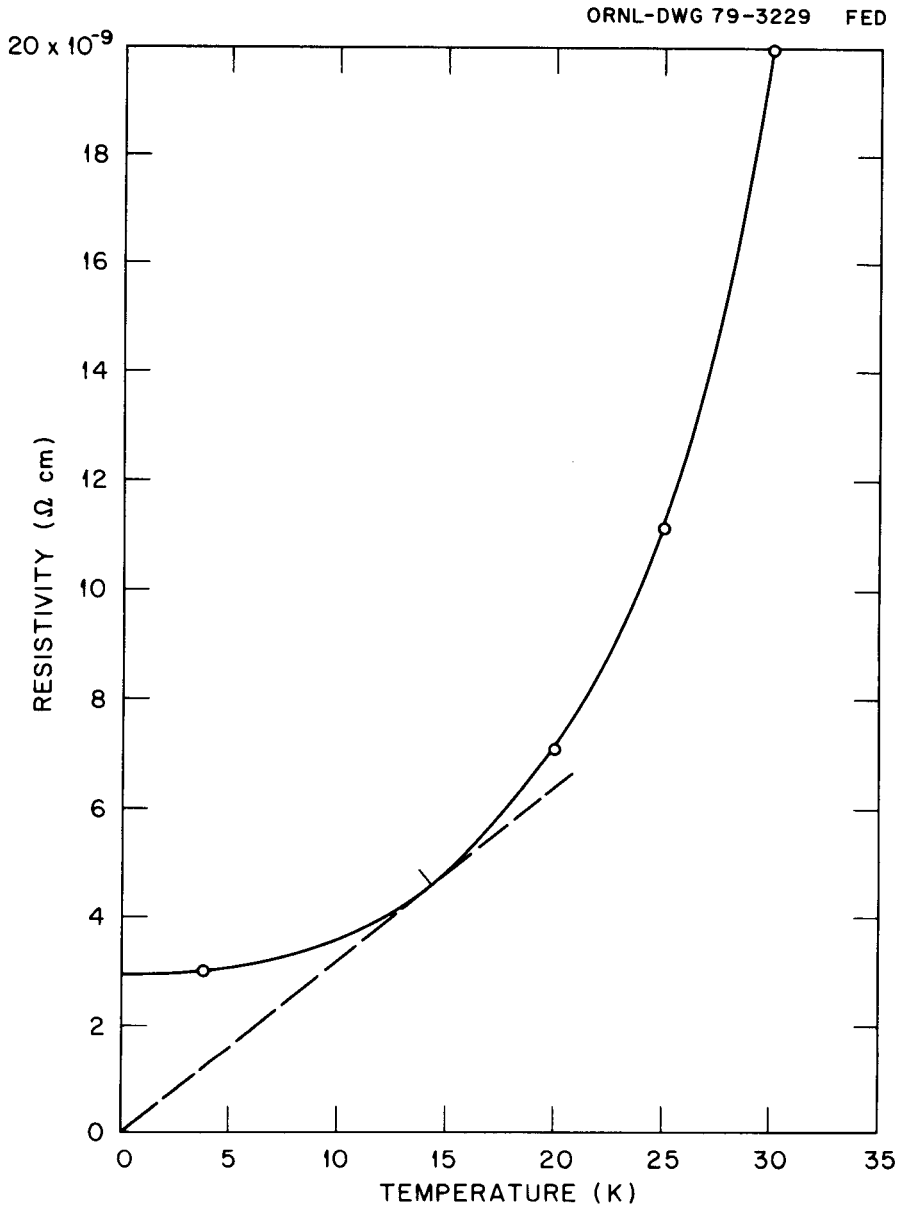


Fig. A1.3. Resistivity of ultrapure aluminum at 4 T. The tangent to the curve (dotted line) indicates an optimum temperature of ∿14.2K.

Table A1.1. Calculated values of Eq. (A1.3) for various temperatures

| Temperature | $\frac{d(1/\sigma)}{dT_L}$ | $\frac{1}{\sigma T_L}\left[\frac{T_H/T_L}{(T_H/T_L) - (1 - \kappa)}\right]$ |
|---|---|---|
| 10K | $1.44 \times 10^{-10}$ | $3.69 \times 10^{-10}$ |
| 15K | $3.2 \times 10^{-10}$ | $3.32 \times 10^{-10}$ |
| 20K | $5.6 \times 10^{-10}$ | $2.96 \times 10^{-10}$ |
| 25K | $10.6 \times 10^{-10}$ | $4.76 \times 10^{-10}$ |

Table A1.2. Energy consumption for different materials

| | Room temperature copper | Room temperature aluminum | Cryogenic aluminum |
|---|---|---|---|
| $1/\sigma$ | $2 \times 10^{-6}\ \Omega$ cm | $2.8 \times 10^{-6}\ \Omega$ cm | $4.5 \times 10^{-9}\ \Omega$ cm<br>$T_H = 320K$<br>$T_L = 15K$<br>$\kappa = 0.3$ |

# APPENDIX 2

## DETAILED PERFORMANCE ESTIMATES FOR DROPLET CLOUD CONCEPT

### 1. METHOD OF ESTIMATING JET BREAKUP LENGTH

We assume that the droplet flow is established in a region of negligible magnetic field, which allows us to evaluate the jet breakup length from data on incompressible flow. Reference 1 presents a summary of empirical data on the breakup of jets of liquid issuing from round nozzles into a region where the gas density is low enough that the jet behavior is unaffected. [Such a jet is sometimes called a free jet (in contrast to a submerged jet, which issues into a region filled with the same fluid).] The data correlate the dimensionless breakup length, $\lambda$, as a function of the Weber number for the jet, $We_j$. The correlation for turbulent jets is

$$\lambda = L/d = 55 + 1.085 \sqrt{We_j} \ ,$$

where L is the jet breakup length, d is the jet diameter (d = 0.25 cm), and

$$We_j \equiv \rho_j (v^2 d/\tau) \ ,$$

where $\rho_j$ is the jet density ($\rho_j$ = 500 kg/m$^3$), v is the jet velocity (v = 166 m/sec), and $\tau$ is the surface tension ($\tau$ = 0.365 N/m). This correlation yields a breakup length, L, of 0.97 m. It seems reasonable to place the nozzles at least this far from the beginning of the magnetic field. If the breakup length is substantially greater than 0.97 m, there appears to be no reason why continuous jets could not be used.

## 2. METHOD OF ESTIMATING REQUIRED DENSITY AND SPACING OF DROPLETS

We assume that all the space in the droplet cloud consists of cubes, each containing a 0.25-cm-diam droplet that occupies 1% of the volume of the cube. This means that each cube must have an edge dimension of 0.94 cm.

For a particle (ion) traveling in a straight line, the probability of hitting a droplet is the area ratio, 0.056. The probability of the particle not hitting a droplet after passing through n cubes is $0.094^n$. If an acceptable value of $0.094^n$ is taken to be 0.01, then n = 80. Given the cube edge dimension of 0.94 cm, we find that the total thickness of the droplet cloud in the direction of ion travel, $t_c$, should be 80 x 0.94 cm, or 75 cm.

## 3. METHOD OF ESTIMATING THE EFFECT OF LORENTZ FORCES ON THE DROPLETS

In order to estimate the effect of Lorentz forces on the droplets, we must approximate the magnetic field strength in the droplet cloud region. Reference 2 estimates the scrape-off thickness for a circular plasma as 20% of the limiter radius, $r_L$, and also describes the approximate configuration bounding the diverted flux region in a cross section of the plasma diametrically opposite the bundle divertor, as shown in Fig. A2.1.

The scrape-off thickness of 0.2 $r_L$ means that the annulus occupies 36% of the total plasma area. We estimate that the diverted flux region occupies one-sixth of the annulus area; thus, it occupies 6% of the total plasma area, or 0.43 $m^2$ for TNS.

Expanding the diverted flux lines to permit energy collection at a heat flux of 1 $kW/cm^2$ requires a collector area of 23 $m^2$. When the flux lines are expanded to this area, the product of area and magnetic field strength must be constant. If we assume that the field strength in the diverted flux region (the shaded area in Fig. A2.1) is 4 T, then we may estimate the uniform magnetic field strength in the collector area, $B_o$, as

$$B_o = 4\ T \times (0.43\ m^2/23\ m^2) = 0.075\ T\ .$$

ORNL-DWG 79-3230 FED

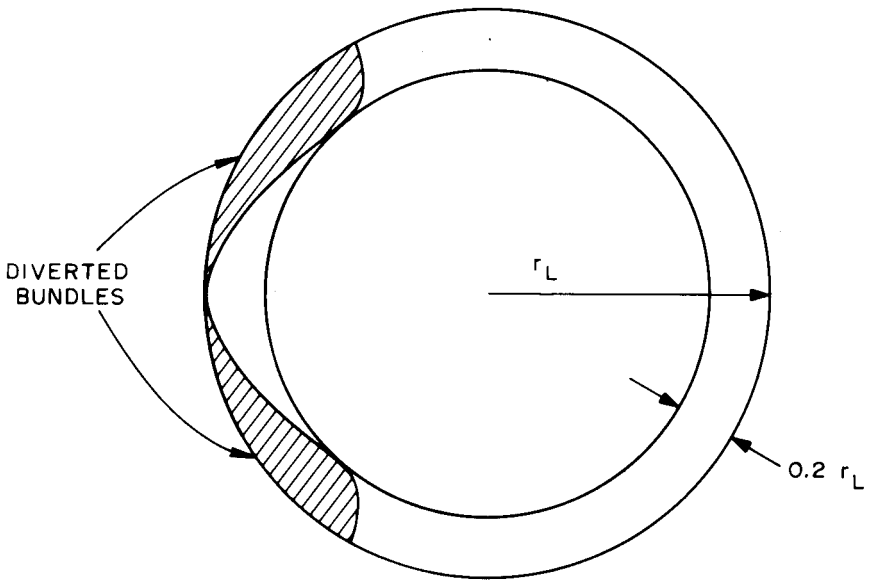


Fig. A2.1. Cross section of circular plasma opposite bundle divertor, showing scrape-off thickness and diverted flux bundle.

Means for approximate analysis of the effects of this magnetic field on the droplets are derived in Ref. 3.

To estimate the change in velocity, $\Delta v$, caused by passing through the magnetic field, we use an equation from Ref. 3,

$$\Delta v = \pi^2 r_d^2 \sigma B_o^2 / 40 \rho L \ ,$$

where $r_d$ is the droplet radius ($r_d$ = 0.125 cm), $\sigma$ is the electrical conductivity ($\sigma = 2.86 \times 10^6$ mho/m), $\rho$ is the lithium density ($\rho$ = 500 kg/m$^3$), and L is the field entry length (assumed to be 1 m). Substitution yields a result of $\Delta v = 1.24 \times 10^{-5}$ m/sec, which is negligible compared with the assumed velocity, v = 166 m/sec.

To estimate the distortion of a droplet by the magnetic field, we use another equation from Ref. 3, which calculates the ratio of the change in magnetically induced pressure, $\Delta p$, to the pressure induced by surface tension forces, $p_\tau$,

$$\frac{\Delta p}{p_\tau} = \frac{r_d^3}{8\tau} \sigma v B_o \frac{\partial B_o}{\partial z} \ ,$$

where $\tau$ is the surface tension ($\tau$ = 0.365 N/m) and $\partial B_o/\partial z$ is the field gradient ($\partial B_o/\partial z$ = 0.075 T/m). Substitution yields a dimensionless result of $\Delta p/p_\tau$ = 0.00178, which indicates that droplet distortion is negligible.

To estimate the transverse displacement, $\Delta y$, of a droplet as it enters or leaves the field, we use a third equation from Ref. 3,

$$\Delta y = r_d^2 L^2 t_c \sigma (\partial B_o/\partial z)^3 / 20 \rho v B_o \ .$$

Substitution yields a result of $1.1 \times 10^{-8}$ m, which is completely negligible.

# 4. METHODS OF ESTIMATING LIMITS ON DROPLET VELOCITY, TEMPERATURE, ION DOSE, AND HEAT FLUX

## 4.1 DROPLET VELOCITY

We assume that the droplet velocity is limited by the supply pressure, which is somewhat arbitrarily set at 6.89 MPa (1000 psi). This is viewed as an approximate practicability limit. We then assume lossless acceleration from this high pressure, negligible velocity condition and convert the pressure into kinetic energy. The resulting velocity is 166 m/sec.

## 4.2 TEMPERATURE

Several factors are taken into consideration in the setting of the peak temperature of the lithium. If we assume that the vapor pressure associated with the hottest lithium zone appears throughout the plasma, then using $10^{-5}$ torr as the vapor pressure limit[4] gives us a peak temperature of about 340°C. However, consideration of the actual conditions in the cloud, the bundle divertor geometry, and the mass flow rate indicates that this assumption is overly pessimistic.

We anticipate that a significant fraction of the droplet cloud will be at temperatures well below the peak temperature. The result should be a vapor flow between the hotter and cooler regions, with a consequent reduction in the vapor pressure away from the cloud.

Inspection of the bundle divertor geometry (see Fig. 5.4 of this report) shows that the area of the magnetic expansion horns is much greater than that of the divertor throats. Also, it is assumed that the walls of the divertor can be maintained at room temperature. Thus, assuming vapor flow (as discussed above) in the molecular regime, we expect that very little of the lithium vapor will enter the plasma region. (This appears to be an advantage unique to the bundle divertor.)

We may calculate the mass flow rate from a hot lithium surface to a region of low pressure with an expression taken from Ref. 5,

$$G = 5.833 \times 10^{-2} p \sqrt{m/T} ,$$

where G is the mass flux from the surface (in g/cm$^2$ sec), p is the pressure (in torr), m is the molecular weight, and T is the absolute temperature. If T = 500°C, then the flux from the lithium-free surface is G = 2.5 x 10$^{-5}$ g/cm$^2$ sec. We apply this to the 2.7 x 4.2 m area on either side of the target area of the divertor and find that 5.7 g/sec is collected on the cold surface. To regenerate this surface, the divertor can be valved off and the surface heated. A temperature of 600°C would produce a mass flux 13 times greater than that for 500°C; because this applies to the large area of the horns, the mass flow rate should be much greater than the 5.7 g/sec above. Gravity flow may be a stronger mechanism for removing lithium from the heated walls.

Other factors considered in determining the peak temperature are the desire to have temperatures that are useful in a thermodynamic cycle and the minimum useful temperature. The temperature selected, 500°C, allows for a temperature rise of 264°C from a minimum of 236°C (the melting point of lithium plus 50°C).

## 4.3 ION DOSE

We assume that the total heat load for TNS, 226 MW, should be distributed so that the heat flux would be no more than 10 MW/m$^2$. The divertor collector surface area (on either side of the target area) is 22.6 m$^2$, as shown in Fig. 5.4 of this report. The ion flow is taken to be 3.5 x 10$^{23}$ ions/sec; combining these values, we obtain a flux of 1.53 x 10$^{18}$ ions/cm$^2$ sec.

Given the droplet cloud velocity of 166 m/sec, the time for the cloud to pass through the target area is 0.016 sec. This leads to a fluence per pass of 2.45 x 10$^{16}$ ions/cm$^2$, which is very low compared with the ion dose of 2.2 x 10$^{18}$ ions/cm$^2$ reported in Ref. 6.

## 4.4 HEAT FLUX

Classical transient heat conduction analysis was used to approximate the heat flux absorption capability of the droplet cloud. The problem needing analysis, that of a sphere with a surface heat flux on one side, was approximated by a cylinder having a diameter and a length equal to the sphere diameter and heated only on one face. This is the traditional slab problem.

We wish to be able to limit the temperature rise to a predetermined value and therefore use a limiting case for the slab problem, the semi-infinite solid solution. For this case, we apply the relation

$$\frac{\dot{q}''}{k\Delta T} = \frac{1}{2}\sqrt{\frac{\pi}{\gamma t}} ,$$

where $\dot{q}''$ is the surface heat flux, k is the thermal conductivity, $\Delta T$ is the temperature rise at the heated surface, $\gamma$ is the thermal diffusivity, and t is the duration of the heat flux.

Our objective is to maximize $\dot{q}''$ for a specific value of $\Delta T$. The duration of the heat flux is determined by the droplet velocity, 166 m/sec, and the flight distance, 2.7 m; we assume that the heat flux is uniform over this distance, so t = 0.016 sec. To estimate the effect of highly peaked heating, we set t equal to the time required to traverse 10% of the flight distance, t = 0.0016 sec. We assign the values k = 46 W/m°C and $\gamma = 2.2 \times 10^{-5}$ m$^2$/sec, take the lithium density as $\rho$ = 500 kg/m$^3$, and obtain the results presented in Table A2.1.

It is clear that the semi-infinite solid solution will underestimate $\Delta T$ and thus yield an overestimate of $\dot{q}''$ for the slab problem. Following Ref. 7, we find that if we take the slab thickness (which represents the sphere diameter) to be 1 mm, the values presented in the table for t = 0.016 sec are 4.2% too high, while those for t = 0.0016 sec are <0.1% too high. For any larger slab thickness, the error is even smaller. Thus, we conclude that for a sphere diameter of >1 mm, our estimates of $\dot{q}''$ are reasonable, and we have assumed a heat flux absorption capability of 1 kW/cm$^2$ for most of our calculations.

Table A2.1. Surface heat flux for two temperature limits

| | $\dot{q}''$ | |
|---|---|---|
| t | $\Delta T$ = 200°C | $\Delta T$ = 400°C |
| 0.016 sec | 1494 W/cm$^2$ | 2749 W/cm$^2$ |
| 0.0016 sec | 4346 W/cm$^2$ | 8692 W/cm$^2$ |

## REFERENCES


1. R. E. Phinney, AICHE J. 21(5), 966 (1975).
2. P. E. Stott, C. M. Wilson, and A. Gibson, Nucl. Fusion 17, 481 (1977).
3. J. S. Walker and W. M. Wells, *Drag Force on a Spherical Drop in a Nonuniform Magnetic Field*, ORNL/TM-6976, Oak Ridge, Tennessee (1979).
4. T. F. Yang, A. Y. Lee, and G. W. Ruck, *Westinghouse Compact Poloidal Divertor Reference Design*, WFPS-TME-042, Westinghouse Fusion Power Systems Department, Pittsburgh, Pennsylvania (August 1977).
5. S. Dushman, *Scientific Foundation of Vacuum Technique*, John Wiley, New York, 1940.
6. G. M. McCracken and S. K. Erents, *Nuclear Fusion Reactors (Proc. British Nuclear Energy Society Conf.)*, p. 353 (1970).
7. H. S. Carslaw and J. C. Jaeger, *Conduction of Heat in Solids*, 2nd ed., Sect. 3.8, Clarendon Press, Oxford, England, 1959.

ORNL/TM-6727
Dist. Category UC-20 d

## INTERNAL DISTRIBUTION

1. W. R. Becraft
2. L. A. Berry
3. E. E. Bloom
4. T. G. Brown
5. D. D. Cannon
6. J. L. Dunlap
7. W. A. Houlberg
8. T. J. Huxford
9. M. S. Lubell
10. J. W. Lue
11. O. B. Morgan
12. Y-K. M. Peng
13. R. L. Reid
14. M. W. Rosenthal
15. C. Sardella
16. J. L. Scott
17. T. E. Shannon
18. J. Sheffield
19. D. Steiner
20. J. S. Watson
21-31. W. M. Wells
32. G. W. Wiseman
33-34. Central Research Library
35-36. Fusion Energy Division Library
37. Fusion Energy Division Communications Center
38-39. Laboratory Records Department
40. Laboratory Records, ORNL-RC
41. ORNL Patent Office
42. Document Reference Section

## EXTERNAL DISTRIBUTION

43. D. J. Anthony, General Electric Co., Bldg. 23, Rm. 290, 1 River Rd., Schenectady, NY 12345
44. J. E. Baublitz, Office of Fusion Energy, Department of Energy, Washington, DC 20545
45. D. S. Beard, Office of Fusion Energy, Department of Energy, Washington, DC 20545
46. S. L. Bogart, Science Applications, Inc., 8400 Westpark Drive, McLean, VA 22102
47. R. Botwin, Grumman Aerospace Corp., Bethpage, NY 11714
48. J. D. Callen, Nuclear Engineering Department, University of Wisconsin, Engineering Research Building, 1500 Johnson Drive, Madison, WI 53706
49. J. F. Clarke, Office of Fusion Energy, Department of Energy, Washington DC 20545
50. F. E. Coffman, Office of Fusion Energy, Department of Energy, Washington, DC 20545
51. D. Cohn, Massachusetts Institute of Technology, Cambridge, MA 02139
52. Library, Culham Laboratory, Abingdon, Oxon, OX14 3DB, United Kingdom
53. S. O. Dean, Science Applications, Inc., 2 Professional Drive, Suite 249, Gaithersburg, MD 20760
54. H. W. Deckman, Advanced Energy Systems Laboratory, Government Reasearch Laboratories, Exxon Research and Engineering Co., P.O. Box 8, Linden, NJ 07036

55. C. A. Flanagan, Westinghouse Electric Corp., Fusion Power Systems, P.O. Box 10864, Pittsburgh, PA 15236
56. H. K. Forsen, Exxon Nuclear Co., Inc., 777 106th Ave., Bellevue, WA 98009
57. H. P. Furth, Princeton Plasma Physics Laboratory, Princeton University, P.O. Box 451, Princeton, NJ 08540
58. R. W. Gould, Mail Stop 116-81, California Institute of Technology, Pasadena, CA 91125
59. R. Hancox, Culham Laboratory, Abingdon, Oxon, OX14 3DB, United Kingdom
60. C. R. Head, Office of Fusion Energy, Department of Energy, Washington, DC 20545
61. R. L. Hirsch, Exxon Research and Engineering Co., P.O. Box 101, Florham Park, NJ 07932
62. M. A. Hoffman, Lawrence Livermore Laboratory, P.O. Box 808, Livermore, CA 94550
63. Anthony Hsu, Office of Fusion Energy, Department of Energy, Washington, DC 20545
64. D. L. Jassby, Princeton Plasma Physics Laboratory, Princeton University, P.O. Box 451, Princeton, NJ 08540
65. V. A. Maroni, Argonne National Laboratory, 9700 South Cass Ave., Argonne, IL 60439
66. D. M. Meade, Princeton Plasma Physics Laboratory, Princeton University, P.O. Box 451, Princeton, NJ 08540
67. P. B. Mohr, Lawrence Livermore Laboratory, P.O. Box 808, Livermore, Livermore, CA 94550
68. M. R. Murphy, Office of Fusion Energy, Department of Energy, Washington, DC 20545
69. J. M. Rawls, General Atomic Co., P.O. Box 81608, San Diego, CA 92138
70. P. Reardon, Princeton Plasma Physics Laboratory, Princeton University, P.O. Box 451, Princeton, NJ 08540
71. T. Reuther, Office of Fusion Energy, Department of Energy, Washington, DC 20545
72. M. Roberts, Office of Fusion Energy, Department of Energy, Washington, DC 20545
73. P. H. Sager, Jr., General Atomic Co., P.O. Box 81608, San Diego, CA 92138
74. G. Schilling, Princeton Plasma Physics Laboratory, Princeton University, P.O. Box 451, Princeton, NJ 08540
75. W. M. Stacey, Jr., School of Nuclear Engineering, Georgia Institute of Technology, Atlanta, GA 30332
76. F. Thomas, Grumman Aerospace Corp., Bethpage, NY 11714
77. T. C. Varljen, Westinghouse Electric Corp., Fusion Power Systems, P.O. Box 10864, Pittsburgh, PA 15236
78. S. S. Waddle, Department of Energy, Oak Ridge Operations, P.O. Box E, Oak Ridge, TN 37830

79-89. J. S. Walker, University of Illinois, Urbana, IL 61801

90. J. Willis, Office of Fusion Energy, Department of Energy, Washington, DC 20545
91. W. Wilkes, Mound Laboratories, Miamisburg, OH 45432
92. E. Ziurys, Office of Fusion Energy, Department of Energy, Washington, DC 20545

93. K. Zwilsky, Office of Fusion Energy, Department of Energy, Washington, DC 20545
94. Office of Assistant Manager, Energy Research and Development, Department of Energy, Oak Ridge Operations, P.O. Box E, Oak Ridge, TN 37830

95-231. Given distribution as shown in TID-4500, Magnetic Fusion Energy (Distribution Category UC-20 d, Fusion Systems)